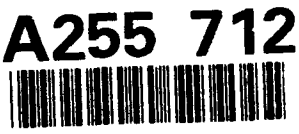

(2)

FINAL TECHNICAL REPORT TO THE OFFICE OF NAVAL RESEARCH

APPLICATION OF RAY-BORN SCATTERING AND BOUNDARY PERTURBATION METHODS TO ACOUSTIC REVERBERATION

GRANT NO. N00014-89-J-3011

15 June 1989 — 30 September 1991

M. Nafi Toksöz
Principal Investigator

Earth Resources Laboratory
Department of Earth, Atmospheric, and Planetary Sciences
Massachusetts Institute of Technology
Cambridge, MA 02139

August 1992

PREFACE

In this project, two theoretical/computational approaches are developed, allowing a detailed study of scattering from various two-dimensional, highly irregular interfaces and from three-dimensional heterogeneous and anisotropic media. Specifically, a two-dimensional staggered grid, finite-difference scheme is adapted to an acoustic-elastic irregular boundary. Comparison with experimental results, using our in-house ultrasonic water tank, show that these finite-difference results accurately predict the amplitudes of waves reflected and diffracted from the interface. This report is a manuscript titled "Reflections from a randomly grooved interface: Ultrasonic modeling and finite-difference calculation", submitted to the Journal of the Acoustical Society of America (1992) by Craig Schultz and M. N. Toksöz.

ABSTRACT

This study utilizes ultrasonic water tank modeling to examine three-dimensional scattering trends from a random set of parallel grooves, and compares this with theoretical results obtained from two-dimensional finite-difference calculations. Ultrasonic laboratory modeling is carried out using computer-controlled source and receivers with an aluminum bock submerged in a water tank. The block's upper interface is plane for the reference model and grooved for the test model. The grooves measure about one-third the center source wavelength and have a Gaussian distribution with a mean of 1 wavelength and a standard deviation of 1/3 wavelength. This experiment places both the source and receiver at the water's surface with the receiver array in the horizontal plane. The receiver line is then positioned at various angles to grooves. A staggered-grid finite-difference scheme is used for theoretical computations and comparisons with laboratory data. These theoretical results matched experimental data well for both the plane interface and the grooved model. Specifically, this study shows that scattering mechanisms are different for propagation normal to grooves than those parallel to the grooves. In the first case scattering takes place in the form of point diffractors. This causes reduction of the specular reflections. Amplitudes decrease by more than 60%, relative to a plane interface, when the incidence angle exceeds 45°. "Snapshots" of finite-difference synthetics helped to clarify details of scattering. In the second case, where the wave front is parallel to the grooves, scattering takes e form of guided head waves and continuous diffractions giving rise to constructive and destructive

interference. This gives the illusion of "broken" reflectors at depth. Amplitude differences appear as large oscillations about a zero mean as head waves refract individually along each groove radiating energy back into the sagital plane.

INTRODUCTION

The scattering of a seismic wave from irregular interfaces has become a topic of critical importance in understanding nonuniform, low amplitude arrivals which tend to complicate ocean seismograms. A number of basic theoretical approaches have been developed to model this scattering. When interface irregularities are small with respect to the seismic wavelength, small perturbations to velocity and density allow a single scattering approximation. Kennett (1972) and Kuperman and Schmidt (1989) have applied the Born approximation to 2-D cases. Prange (1989) has perturbed material parameters and interface height to describe 3-D scattering from randomly rough interfaces in terms of simple matrix operators. Both techniques have the advantage of separating the scattered wavefield from the background field. However, when the size of an interface irregularity approaches the incoming wavelength and impedance contrasts are large, the above approximations break down and complete waveform modeling must be introduced to understand the multiply scattered waves. This involves implementing full waveform numerical techniques such as the discrete wavenumber-boundary integral (Bouchon *et al.,* 1989), boundary element (DeSanto, 1985; Campillo and Bouchon, 1985; Paul and Campillo, 1988), or finite-difference (Virieux, 1986; Bayliss *et al.*, 1986; Stephen, 1988) methods. Stephen (1988) gives an excellent summary of current acoustic-elastic finite-difference techniques, and Axilrod *et al.* (1990) compares run time and accuracy between the various discrete wavenumber techniques. Although computational constraints usually require two-dimensionality, spreading factor corrections can

give reasonable amplitude data for comparison with three-dimensional point sources. Unfortunately, the inability of full waveform techniques to model three-dimensionally irregular interfaces is difficult to avoid. In this respect ultrasonic modeling has become an important tool for 3-D modeling, approaching the geometrical, source, noise, and material property control enjoyed by the numerical techniques above.

This study utilizes ultrasonic water tank modeling to examine three-dimensional scattering phenomena from a random set of deeply cut parallel grooves, labeled as a "random diffraction grating," and compares them with theoretical results obtained from numerical calculations. These grooves measure about one-third the incoming wavelength and have a Gaussian spatial distribution. These properties place the interface in the "full waveform zone" of Aki and Richard's scattering classification (Aki and Richards, 1980). Finite-difference modeling is therefore incorporated in the two-dimensional scattering case, with a seismic line perpendicular to groove strike. These synthetics also avoid the source-receiver effects that arise in the experimental data. Amplitude versus distance *(AVD)* curves then sow the reflected amplitude variations in both the two- and three-dimensional grooved cases.

The random diffraction grating, in this case with "V" shaped grooves, may be related to many different structural regions. In extensional zones, such as the Basin and Range province of the western United States, extensive normal faulting occurs over short distances. This may leave jagged boundaries between the layers severed by faulting. Mid-ocean ridges and continental rifting areas with extensional faulting may similarly result in irregular interfaces,

giving the effect of elongated grooves. In addition, poorly understood deep boundaries, such as the Mohoroviĉiĉ discontinuity, may be highly irregular, possibly explaining coherent noise encountered on short-period seismograms. Similar situations exist in all frequency ranges including the ultrasonic range investigated here.

ULTRASONIC MODEL DESCRIPTION

Ultrasonic modeling is carried out in our in-house water tank, where computer-controlled transducer holders can move the source and the receiver in all coordinate directions. An aluminum block with 30 × 30 cm area and 15 cm height is used as the ultrasonic tank model. This model has physical properties similar to upper crustal rocks, thus giving a large impedance contrast with water and large reflected amplitudes.

Figure 1 shows a two-dimensional view of the block studied. Figure 1a shows the control case with a plane interface on both the upper and lower boundaries. Figure 1b illustrates the block with an irregular upper interface. The interface consists of parallel "V" shaped grooves, each with a constant depth of 3 mm and a 60° lower acute angle. The grooves form a Gaussian distribution with a 1 cm average standard deviation of 3 mm, and the constraint that grooves do not overlap. Due to this spatial randomness the interface is termed a "random diffraction grating." Although the slope discontinuities and steepness of each groove allow for local multiple scattering effects, we focus only on the interference caused by the groove distribution as a whole.

EXPERIMENTAL METHODS

Ultrasonic water tank modeling involves submerging a structure, in this case the aluminum block described above, in a water tank. Although the tank is of finite dimension, any reflection from its sides arrives outside the desired time window. Piezoelectric transducers act as the source and receiver. A vertically polarized cylindrical transducer generates the sharp pulse that is important in resolving multiple scattered trends. However, in making the source impulsive, the source radiation pattern becomes a strong function of the angle from the axis. This pattern will be important later in comparing experimental amplitudes with synthetic results. For now we only note that a large amplitude oriented downward in the radiation pattern renders amplitudes in the first few traces useless. These traces are therefore muted from the ultrasonic results.

Placing the transducers just beneath the surface eliminates scattering from the source and receiver supports. Unfortunately, this source position distorts recorded wave amplitudes as the incident and surface reflected waves interact near the receiver. The analysis of this effect discussed in detail in the next section, shows that, although the surface distorts the appearance of the seismogram as a function of source receiver separation, it has little effect on the comparison of relative amplitudes between different interfaces.

The experiments involve a single source and a line of multiple receivers. As shown in Figure 1, the source is positioned over the interface, 5 cm from the block's edge. The receiver array begins at the source and extends 5 cm past the opposite corner with 2.85 mm

spacing. The source wavelet is a narrow band pulse with 0–300 kHz frequency range and peak amplitude at 185 kHz. The center wavelength measures 1 cm and varies from 1.5 to .5 cm over the effective frequency range of the source. The grooves therefore range from one-fifth to three-fifths the width of the incoming wavefield. All traces are averaged over 1.024 source sweeps, reducing random noise amplitudes far below that of the scattered field.

Plane Interface

Figure 2a shows the experimental results from the plane interface control block. The reflected wave appears earliest in the seismogram with the largest amplitude. Other phases are identified by looking at their apparent velocities. Refracted P-wave energy is barely identifiable at this scale, while the shear head wave exhibits much larger excitation. This is common with acoustic-elastic boundaries as normal displacement and normal tractions at the boundary have major components in the direction of shear head wave displacement. Due to its phase shift and large amplitude, this head wave interferes with the reflected wave amplitudes destructively and then constructively over a large distance. Reflected amplitudes cannot be studied in this range.

Following the primary reflection, diffractions occur from both corners of the block. The hyperbolic trend and limiting water velocity at large distances identify the diffraction nearest the source. The opposite corner diffraction appears at about 265 μs. The low energy bottom of the block reflection arrives at 190 μs. Due to the high acoustic impedance, one

reverberation from within the block is also observed at 230 μs. The first water multiple is muted along the top of the seismogram starting at 250 μs.

Grooved Interface

Three groove geometries are studied in this section. We begin by examining the two-dimensional diffraction grating. Turning to the limiting 3-D case, with the grooves parallel to the seismic line, we take advantage of the simplified geometry to understand the different style of scattering. These two limiting cases become very valuable because they form a tool for explaining scattering phenomena observed in the third case, where the grooves strike is diagonal to the source-receiver line.

Perpendicular to the Grooves

Figure 3a shows the seismogram recorded along a receiver line oriented perpendicular to the groove strike. The primary reflected wave still dominates the seismogram. However, its amplitude varies nonuniformly as scattered energy interacts with and trails the initial reflection. These scattered arrivals persist until the seismogram ends. Comparing these traces to those in the plane interface case suggests that the grooves completely obstruct both S and P head wave propagation. Some of this energy most likely appears as time-delayed low energy arrivals.

Scattered energy, immediately following the primary reflection, exhibits distinct trends.

Hyperbolic arrivals (all originating within the primary reflection) appear, paralleling the trend of the corner diffraction identified in the control case. Since each hyperbola follows a point diffractor trajectory with a limiting water velocity, these arrivals appear to be multiple scattered diffractions originating from the grooves. The difficulty in correlating any one diffraction with a specific scatterer suggests that each groove acts as a complex multiple diffractor. Furthermore, the energy coalesces into a narrow wedge of high amplitude trailing the primary reflection, causing a large amount of interference. Although the bottom of the block reflections are still identifiable, the larger amplitude diffractions muffle their presence. Migration may act as a tool in bringing out the bottom of the block reflector as diffractions collapse back into grooved secondary sources.

Parallel to the Grooves

The simplest three-dimensional case arises when the seismic line extends parallel to the groove strike. As shown in Figure 4a, scattered energy appears following a large amplitude reflection from the irregular boundary. The trends, although taking the form of continuous hyperbolic curves, differ greatly from the two-dimensional situation. The hyperbolas do not originate within the primary reflected wave. Instead, they intersect the first trace with a distinct time delay and tend to parallel the primary reflection at small offsets. At larger offsets, these trends converge on the primary reflection instead of diverging like the point diffractors in the two-dimensional case. This smears the primary reflected wavelet so that

it shows little similarity to the incident wavelet. The convergence of these hyperbolas to one another results in additional interference, giving the appearance of broken reflectors at depth, not an irregular interface.

The S head wave is still prominent in the profile. At later times secondary arrivals paralleling the initial head wave branch also appear. Each later branch can be traced back to its origin which lies within the trailing hyperbolas described above. This intersection with the hyperbolas smears the constructive-destructive interference between the primary reflected and earliest head wave to larger times.

The above observations suggest that each individual groove acts as a continuous diffractor of energy. The geometry for a continuous groove diffractor allows a number of paths to exist, each having slower moveout than the primary reflected arrival. This explains the observed convergence of individual hyperbolas at large distances. In addition, the parallel head wave arrivals and the extension of constructive head wave interference both suggest that each groove acts as a head wave guide, continuously releasing energy back into the vertical plane of the receiver array.

Diagonal to the Grooves

Utilizing our knowledge from the two limiting cases described above, one can understand scattered trends recorded at intermediate receiver array azimuths. We now describe the trends on a seismic line positioned diagonal to the grooves.

Figure 4b shows the seismic data recorded with a receiver line oriented 45° to groove strike. The trends display more complexity than the first two cases. The primary reflection contains the largest amplitude, and scattered arrivals again form hyperbolic trends. Some hyperbolas never intersect the primary reflection but instead intersect the first trace with some time delay. Other trends originate within the primary reflection and appear more as point diffractions from the interface. In both cases the hyperbolas are divergent from the primary reflection branch, with a slope between the limiting cases studied previously. Head waves also appear, but they dissipate within a few traces after they are formed.

The two limiting cases above suggest an explanation for these observed trends. Components of both cases are clearly present, suggesting that scattering from a random diffraction grating can be explained in terms of the multiple point diffraction and head wave obstruction observed in the two-dimensional case along with the continuous diffraction and head wave guidance for the case parallel to the grooves. More specifically, shooting diagonal to the grooves gives the appearance of 45° dipping reflectors at depth as each groove continuously diffracts energy. However, some diffractions give the impression of interface origin. The slight persistence of head waves suggests that energy radiates into the sagittal plane as groove-guided refractions cross underneath the receiver line. Head waves propagating parallel to the seismic line are obstructed.

Amplitude Versus Distance

In this section we investigate how a random diffraction grating changes reflected wave amplitude with distance from the source. *AVD* curves for the grooved interface are compared with the amplitude curve for a plane reflector. More useful, however, is the "relative difference" in amplitude between the plane and grooved reflection. This gives an accurate measure of amplitude variation induced by the random diffraction grating.

Figure 5a shows the *AVD* curve for the plane layer control case. Destructive and constructive interference of the shear refraction affects amplitudes from the critical angle at 30° to about 40°, as marked on the graph. In the scattered cases, this destructive null and constructive buildup is greatly reduced, causing amplitude differences as high as 100% in this range. Therefore, amplitudes in this region are not studied. The measured amplitude over the two-dimensional grooved interface is also shown. Comparing the primary scattered reflection to the control case reveals a decrease in reflected amplitudes at most offsets. The reflection amplitude rises above the control case only during the S head wave interference zone. Notice that the grooved interface also appears to shift the head wave interference zone to larger incident angles. (Part of this offset appears to result from a difference in velocity between the two blocks and will be corrected in any future work. However, another portion of this offset may also represent anisotropy created directly by the grooved interface. This is supported by the smaller lag in crossover distance when shooting diagonal to the grooves in the next section.) The relative difference between the two curves, also shown in Figure 5a,

strongly depends on offset. Waves near normal incidence lose an average of 10–15% of their amplitude. At angles greater than 40° the difference quickly climbs to values as large as 60%. Clearly, increasing the incident angle greatly reduces reflected amplitudes.

Figure 5b plots the AVD curves for the three-dimensional geometries studied. In the limiting case, parallel to groove strike, an average of 15% loss in amplitude is recorded at small incident angles, most likely resulting from interference with diffractions from the nearest grooves. At larger angles, amplitudes start oscillating rapidly about the plane AVD curve causing relative differences larger then 80%. This oscillation is apparently due to the multiply refracted S head wave arrivals crossing the primary reflection. Turning to the intermediate case, with grooves striking 45° under the seismic line, scattering causes reflected amplitudes to rise by about 15% at lower incident angles. The amplitude decreases below the control case only after the refractive critical angle. At large angles amplitudes are very similar to the two-dimensional case, approaching 50–60% lower amplitude at angles greater then 45°.

In all cases, the AVD curves establish 10–15% amplitude variations at low angles of incidence. Increasing the incident angle reduces amplitudes by as much as 60%. Although this maximum deviation of 60% appears similar between models, AVD signatures vary greatly between different groove azimuths.

COMPARISON WITH FINITE-DIFFERENCE

Two-dimensional finite-difference techniques allow full waveform modeling in both water and the aluminum block. In addition, source-receiver distortions, which noticeably affect experimental data, are not present in these synthetics. In the next section we investigate the nature of distortions present in the experimental tank. These distortions are then applied, using various approximations, to the finite-difference synthetics. Amplitudes are then compared to the experimental results of the previous section.

Finite-Difference Algorithm

One of the fundamental problems with the finite-difference technique occurs when modeling a sharp interface between two media with widely varying elastic constants. Two difficulties in particular arise when dealing with the acoustic-elastic boundary on a non-staggered grid. First, a boundary condition with continuous normal stress and displacement must be applied. For a non-staggered grid this boundary condition must be set up artificially by the programmer. Second, large impedance contrasts can cause large instabilities at the interface rendering some results useless (Stephen, 1988). Fortunately, the staggered grid solves these two problems naturally by offsetting horizontal and vertical displacement grids; no explicit boundary condition is required. However, the boundary condition is not absolutely abrupt and is approximated over one finite grid spacing, allowing some averaging to occur. The models in this paper were created using a stress-displacement finite-difference algorithm.

This algorithm was adapted to an nCUBE2 multiple instruction, multiple data, parallel processor.

This staggered-grid scheme is stable for the high impedance contrast, acoustic-elastic boundary encountered in this study. First-order absorbing boundaries developed by Lindman (1975) and later introduced to geophysics by Randall (1989) are implemented. These boundaries give reflection amplitudes less then one percent the incident wave amplitude at all angles less then 90°.

The synthetic model parameters were chosen to minimize grid dispersion. The grid measures 960 by 813 points with a grid spacing of .375 mm. The time increment is approximately .03 μs, where the actual sampled time interval is .4 μs. Therefore the shortest wavelength of 5.0 mm is sampled with 13 grid points. The smallest time period is sampled 110 times, which is well within the stability limits. A windowed Ricker wavelet with a 0–300 kHz frequency range and 185 kHz peak amplitude is used to approximate the transducer source wavelet.

Numerical Results

Figure 6 shows two finite-difference time slices of a wave reflecting from the plane-bounded block (Figure 1a). The grey scale plots vertical displacement resulting from a vertical point source and is scaled to one-half the maximum amplitude on the grid. Each feature present in the experimental data is identified in Figure 6. Figure 7 gives similar time slices for the random diffraction grating. Scattered energy takes the form of large amplitude diffractions

trailing the primary reflected wave. A large amount of reverberative energy trapped within the block also results from transmission through the irregular boundary. A few broken multiple head waves project from the primary reflected wave like faint spears. This suggests that each groove acts as its own secondary source for head wave energy, which the remaining grooves quickly obstruct.

Figure 2b presents the synthetic pressure record for the plane-bounded aluminum block and compares this with the experimental recordings. The synthetic emphasizes diffractions and refractions created by the block corners, again demonstrating how a slope discontinuity can create head waves and diffractive waves. Figure 3b illustrates synthetics recorded over the grooved interface. Scattered trends are accentuated. These trends are similar to those observed in the experimental data with a narrow zone of coalescing diffractions trailing the primary reflected wave. Lower amplitude, backscattered energy appears sloping toward a larger offset. Figure 8 gives the pressure field recorded over the same block, but with a volume source. The volume source, in comparison to the vertical point source, creates much greater backscattered diffractive energy at a large offset. Note that, although a three-dimensional spreading factor (discussed below) has been applied to both seismograms, the scattered amplitudes exhibit higher amplitude than the experimental case. Two additional first-order tank distortions must be applied to the finite-difference results before the primary reflected and later scattered arrival amplitudes can be compared to the experimental data of the previous section.

A total of three corrections applied to the volume source synthetics for comparison with experimental data. The first correction accounts for the transducer source radiation pattern and the receiver sensitivity pattern; both vary strongly as a function of inclination. We assume that the energy contributing to the primary reflected amplitude comes from a small zone about the path that a plane-reflected wave would follow. Each trace is multiplied by a single scaling factor based on the transducer source amplitude in the direction of that path. This geometrical correction is valid only in the vicinity of the primary-reflected wave as later scattered arrivals do not follow this assumed path. This correction demonstrates the distortion of experimental scattered arrivals as a function of a ray's emergence from the source. Notice that the amplitude of head waves and the bottom of the block reflections are not properly corrected because these paths also differ from the specular field. The second correction, already implemented above, involves correcting the 2-D synthetic data for 3-D spreading. If the scattered wave travels exclusively in the water, multiplying amplitudes by an $r^{-1/2}$ factor corrects for spreading of the specular wavefield. In this case, r is the total distance traveled in the water.

The third correction factor involves correcting for wavefield interference at the water's surface. The boundary conditions at the free surface give the pressure field near the receiver.

$$P = \exp[-iwt + ik_x x](\exp[ik_z z] - \exp[-ik_z z]), \tag{1}$$

assuming a plane incident wave with wavenumber $\underline{k} = (k_x, k_z)$. Taking z to be small the

pressure depends only on vertical wavenumber and receiver depth,

$$P \propto |k| z \cos(\alpha), \tag{2}$$

where α is the incident angle of the wave impinging on the receiver, measured from normal. Notice that the pressure field goes to zero at the surface as expected. This correction is applied using the geometrical ray angle approximation summarized above for the first correction. Expression (2) shows no amplitude distortion at normal incidence but accounts for one-half the wave amplitude at a 60° incident angle. This corresponds to the last receiver on the profile. Note that the relative difference in amplitude due to scattering is not changed (to first-order) by the above distortions in the tank since the distortions appear as identical multiplicative factors in both the scattered and the plane layer case (the corrections factor out and cancel in the relative difference calculation).

It is important to emphasize that the corrections implemented above apply only in the vicinity of the first-reflected energy. It is difficult to determine the exact path a scattered wave traverses in traveling from source to receiver. Therefore, these corrections hold only near the specular field. Since finite-difference avoids these distortions, it may be useful for future amplitude analysis. However, the correction for spherical spreading is a good approximation only where an unperturbed wave travels exclusively in water. The 3-D spreading of diffractions are also left uncorrected. In addition, waves traveling through any part of the block, such as the bottom of the block reflections, are under-corrected.

Figures 9a and 9b show the two-dimensional experimental AVD curves overlaid on the

corrected finite-difference results. For a plane layer (Figure 9a) the curves agree within 15% at most angles. In the area of head wave interference, rapid changes in amplitude cause larger differences. Comparing the results for the random diffraction grating with the synthetics (Figure 9b), they match very well at wide angles. A larger disagreement, however, occurs at low incident angles where finite-difference predicts greater then 30% lower amplitudes in some regions. These differences may result from rapid changes in the transducer radiation pattern and slight variations between the filtered Ricker wavelet and the transducer wavelet. Figure 9c shows the AVD signature predicted by finite-difference. As expected, finite-difference predicts 5–10% more scattering about the lower incident angles than experimental data. The synthetics support a maximum amplitude change of 60% for wide angle reflections approaching 60°.

DISCUSSION

Ultrasonic water tank experiments reveal that waves scattered from a random diffraction grating can be understood in terms of two simple models. First, in the case where the incoming wavefield travels perpendicular to the grooves, scattering takes place in the form of point diffractors and obstructed refractions. Amplitude variations relative to the the control case of a plane reflector average about 10–15% at lower incident angles (0–20°) and rise as high as 60% at angles greater than 45°. Second, in the case where the receiver array is parallel to the grooves, scattering takes the form of guided head waves and continuous diffractions,

giving the illusion of broken reflectors at depth. The relative differences reach magnitudes similar to the two-dimensional case above. However, at a large offset this difference takes the form of large oscillations about zero as multiple head waves intersect the primary-reflected wave. Diagonal to the grooves, scattering becomes a combination of trends identified in the two limiting cases above, and amplitudes show an AVD signature similar to the two-dimensional case.

Finite-difference modeling gives primary reflected wave amplitudes that match experimental results to within 15% over most angles in both the plane and grooved cases. However, in some small offset regions over the grooved interface, finite-difference predicted 30–40% lower amplitudes than were observed. Larger differences were also observed due to rapid variation in head wave interference zones.

Numerical calculations have since been carried out for models with different velocities, including cases where the shear velocity of the solid is above and below the P-velocity in water. These show distinct trends in amplitude variation and have implications for AVD analysis. Further studies may include the frequency analysis of diffracted and transmitted waves at the interface. In addition, the effect of migration on reducing scattered noise may serve as an interesting test for the resolving power of techniques such as Kirchhoff migration. Although this study keeps groove geometry constant to allow for careful comparison with experimental data, further studies will use more general, random interfaces to study scattering amplitudes and trends.

ACKNOWLEDGMENTS

This research was partially supported by the Defense Advanced Research Projects Agency through contract #F19628-89-K-0020, administered by the Phillips Laboratory (formerly the Geophysics Laboratory) of the Air Force Systems Command and by the Department of the Navy,Office of the Chief of Naval Research through grant #N00014-89-J-3011.

References

Aki, K. and P. Richards, 1980, *Quantitative Seismology—Theory and Methods*, W. H. Freeman, San Francisco, 721–796, 1980.

Axilrod, H.D. and J.F. Ferguson, 1990, SH-wave scattering from a sinusoidal grating: An evaluation of four discrete wavenumber techniques, *Bull. Seism. Soc. Am.*, 644–655.

Bayliss, A., K.E. Jordan, J. LeMesurier, and E. Turkel, 1986. A fourth-order accurate finite-difference scheme for the computation of elastic waves, *Bull. Seism. Soc. Am.*, *76*, 1115–1132.

Bouchon, M., M. Campillo, and S. Gaffet, 1989, A boundary integral equation-discrete wavenumber representation method to study wave propagation in multilayered media having irregular interfaces, *Geophysics*, *54*, 1134–1140.

Campillo, M. and M. Bouchon, 1985, Synthetic SH seismograms in a laterally varying medium by the discrete wavenumber method, *Geophys. J. R. astr. Soc.*, *83*, 307–317.

DeSanto, J., 1985, Exact spectral formalism from rough-surface scattering, *J. Opt. Soc. Am.*, *12*, 2202–2207.

Kennett, B.L.N., 1972, Seismic wave scattering by obstacles on interfaces, *Geophys. J. R. astr. Soc.*, *28*, 249–266.

Kuperman, W. and H. Schmidt, 1989, Self-consistent perturbation approach to rough surface scattering in stratified elastic media, submitted to *J. Acoust. Soc. Am.*

Lindman, E., 1975, Free-space boundary conditions for the time dependent wave equation. *J. Comp. Phys., 18*, 66–78.

Paul, A. and M. Campillo, 1988, Diffraction and conversion of elastic waves at a corrugated interface, *Geophysics, 53*, 1425–1424.

Prange, M.D., 1989, Perturbation approximation of 3-D seismic scattering, submitted to *Geophysical Journal.*

Randall, C., 1989, Absorbing boundary condition for the elastic wave equation: Velocity-stress formulation, *Geophys., 54*, 1141–1152.

Shortt, E.R., 1986, Laboratory borehole modeling, Full Waveform Acoustic Logging consortium, 461–470.

Stephen, R.A., 1988, A review of Finite difference methods for seismo-acoustics problems at the seafloor, *Review of Geophysics, 26*, 445–458.

Tang, X-M., 1989, Elastic wave radiation and diffraction of a piston source, *JASSA*, in press.

Virieux, J., 1986, P-SV Wave Propagation in heterogeneous media: Velocity-stress finite-difference method, *Geophysics, 51*, 889–901.

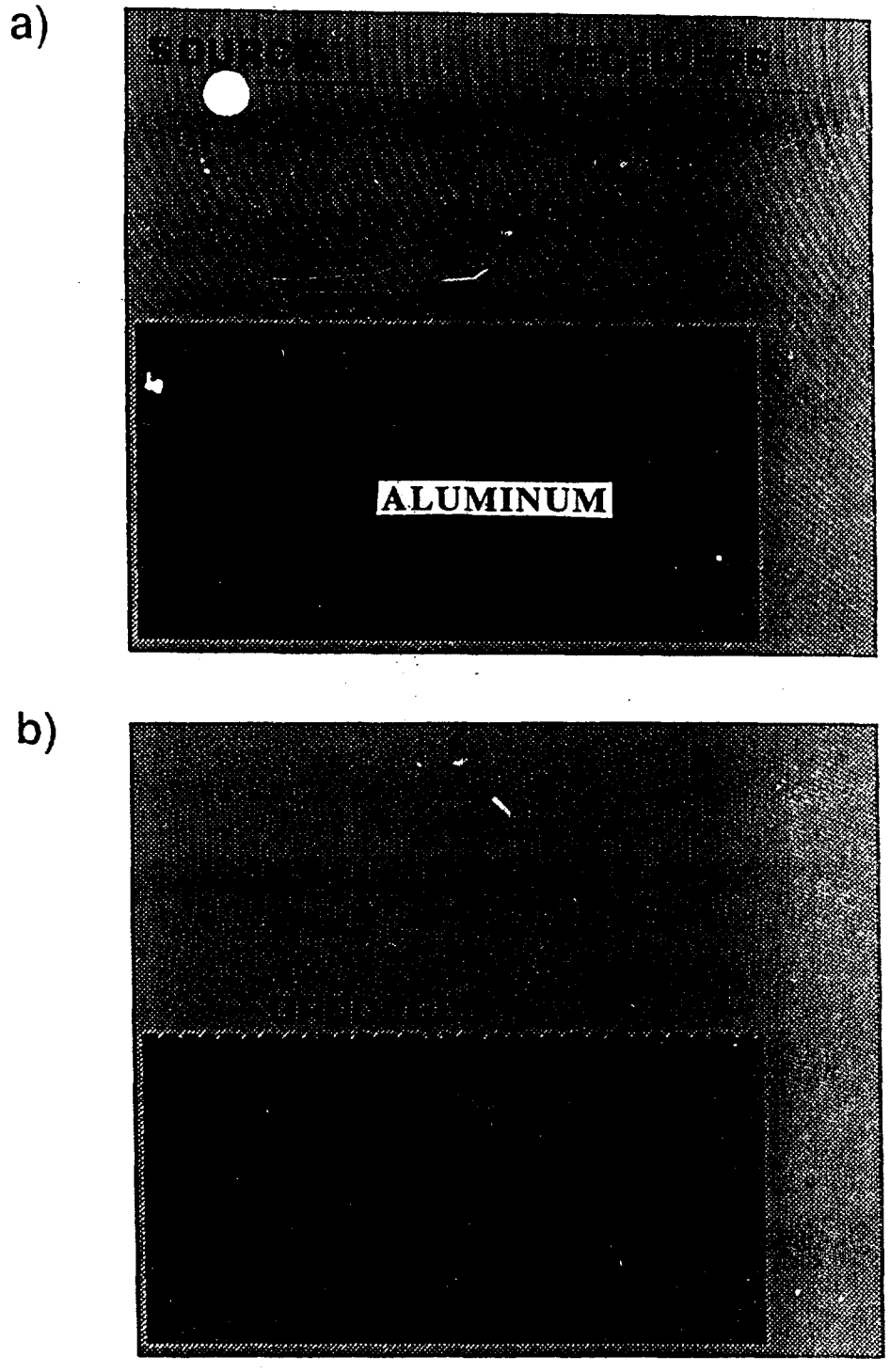

Figure 1: Two-dimensional cross-section of block geometry used for ultrasonic water tank and finite-difference modeling. (a) The control case with an upper and lower plane boundary. (b) The randomly grooved interface, looking down the strike of the grooves. The boundary in both cases is acoustic-elastic.

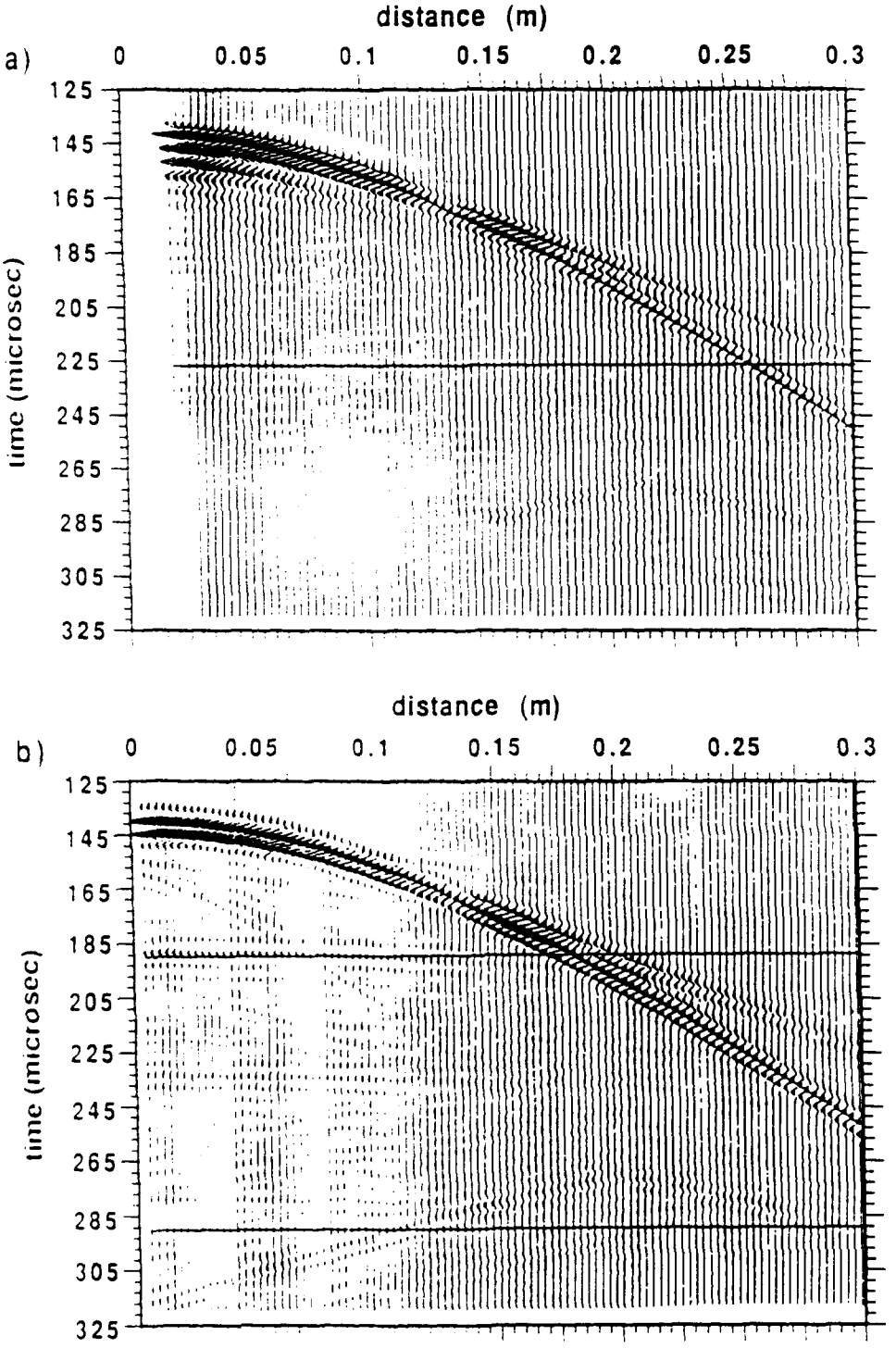

Figure 2: Seismogram recorded 10 cm above the smooth interface using a small pinhead transducer. The record starts at 125 microseconds, truncating the direct arrival. Amplitudes are trace normalized to 1.0 and all recordings over the grooved interface are scaled with this same factor. (a) corresponds to the experimental control case while (b) corresponds to finite-difference synthetics.

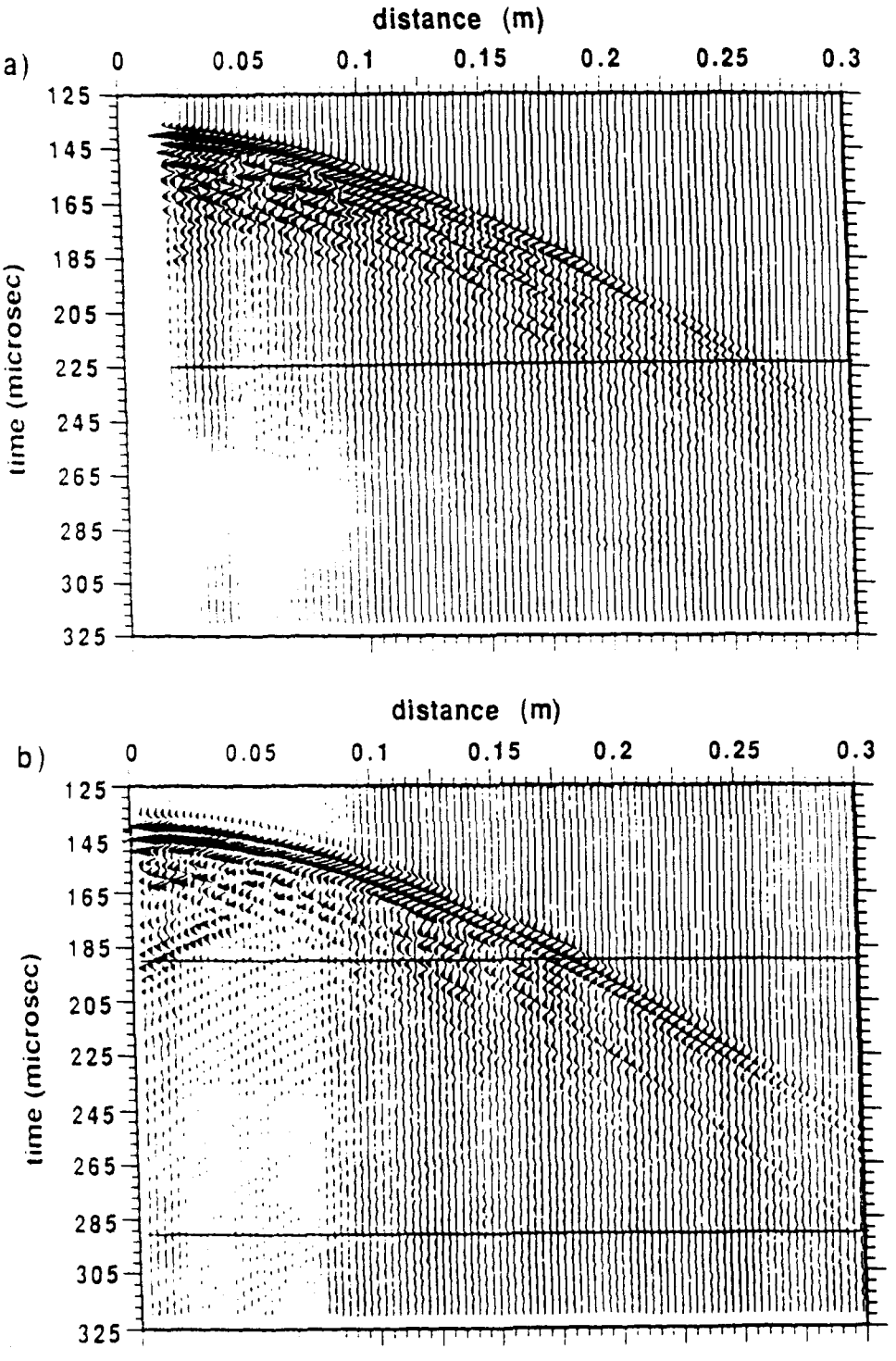

Figure 3: Similar to Figure 2 but for the two-dimensional case with the seismic line oriented perpendicular to the groove strike. (a) corresponds to the experimental results and (b) to the finite-difference synthetics.

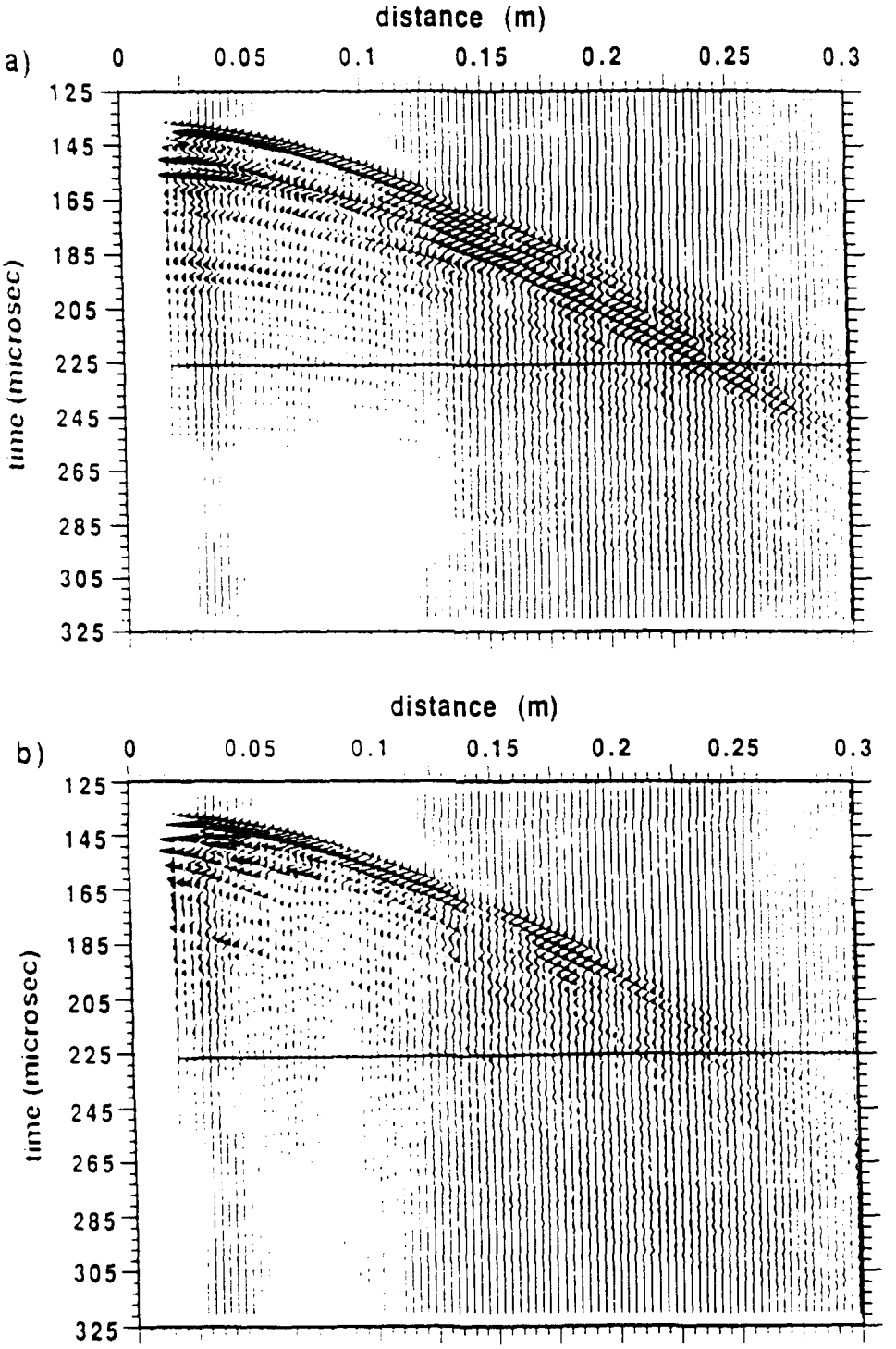

Figure 4: Similar to Figure 2 but for (a) the simplest three-dimensional experimental case with the seismic line parallel to the grooves, and (b) the more complex experimental case of a seismic line oriented at 45° with respect to groove strike.

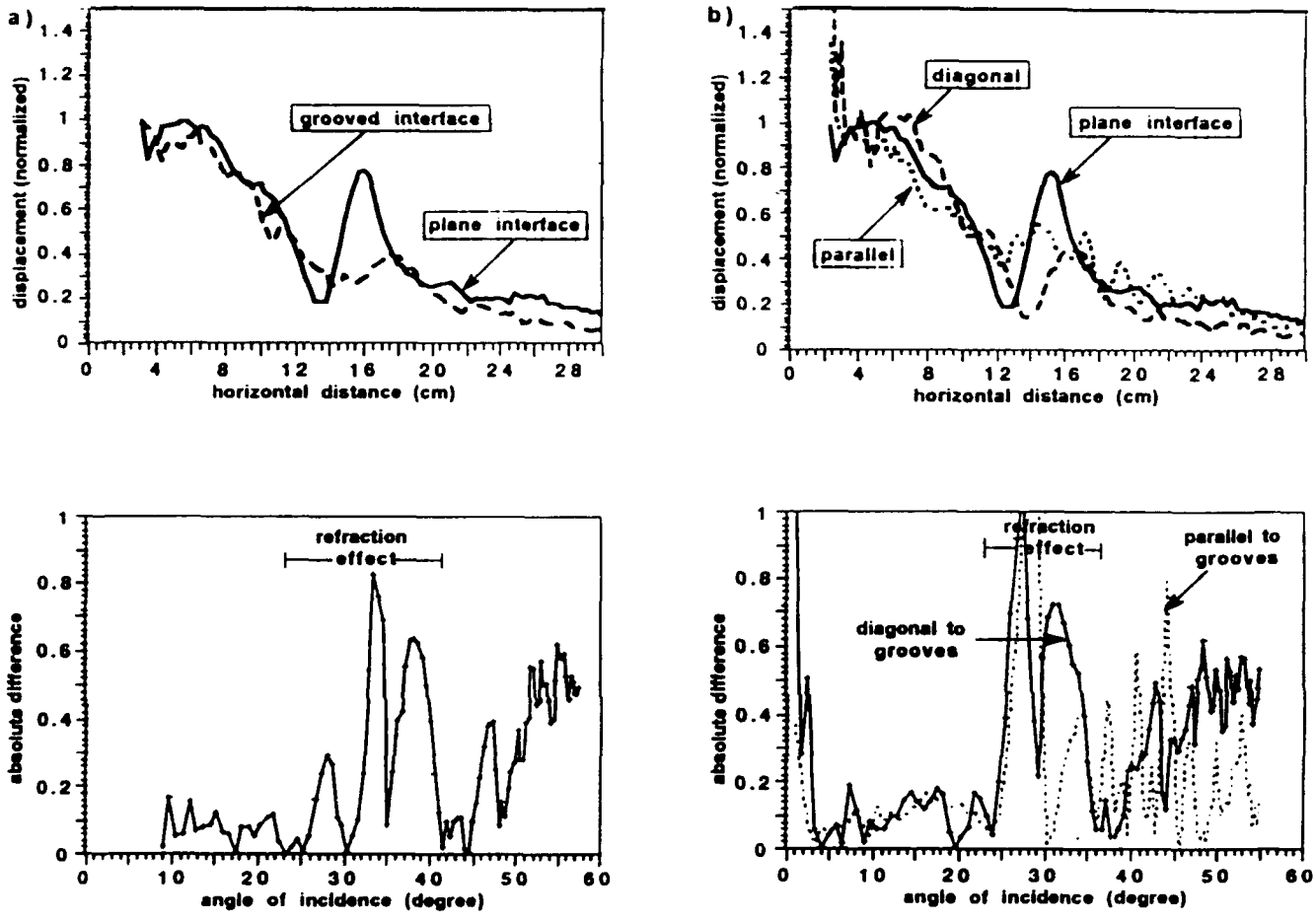

Figure 5: Wavefield amplitude in the acoustic medium versus distance from the source for a primary reflected wave: (a) Plots the experimentally derived curves for both the plane interface and the two-dimensional grooved surface along with their relative difference as a function of incidence angle. (b) is similar to (1), except the curves are for a seismic line oriented both parallel and 45° to groove strike.

a)

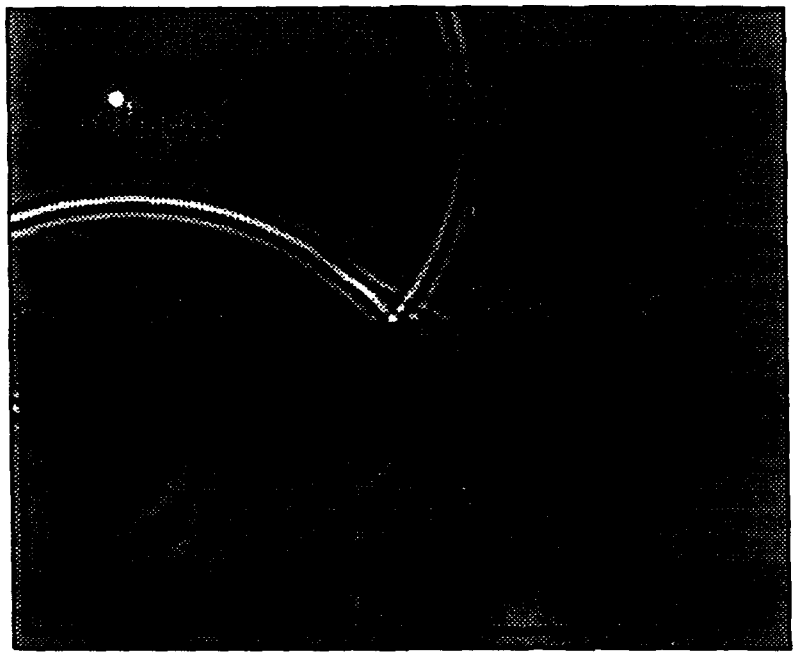

b)

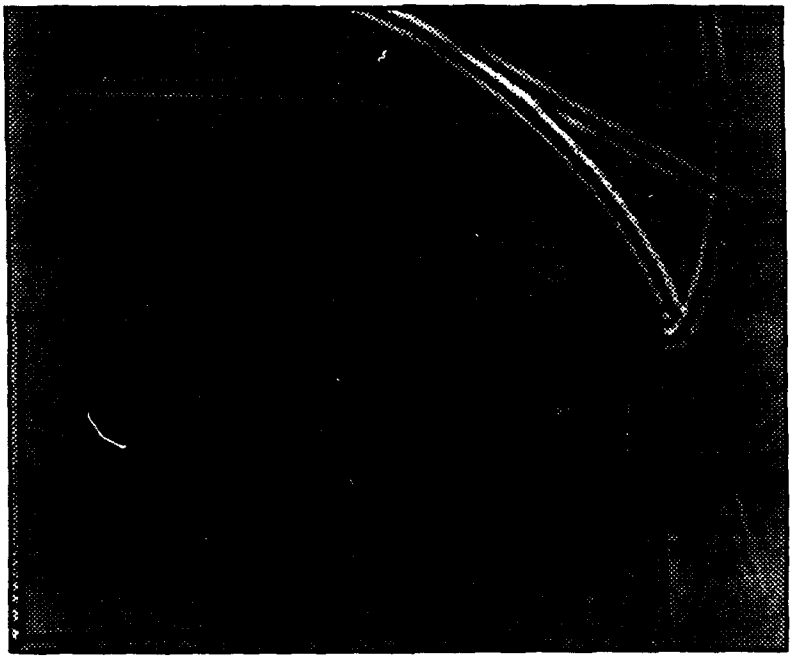

Figure 6: Two finite-difference time slices showing the vertical displacement from a vertical point source. The source receiver geometry is identical to that of the experimental models (Figure 1).

a)

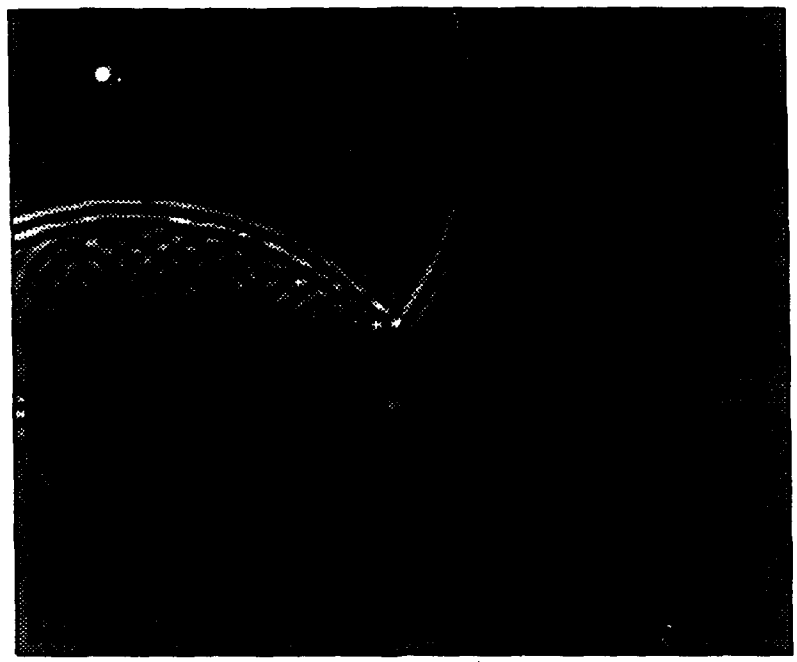

b)

Figure 7: Similar to Figure 6, but for the two-dimensional random diffraction grating.

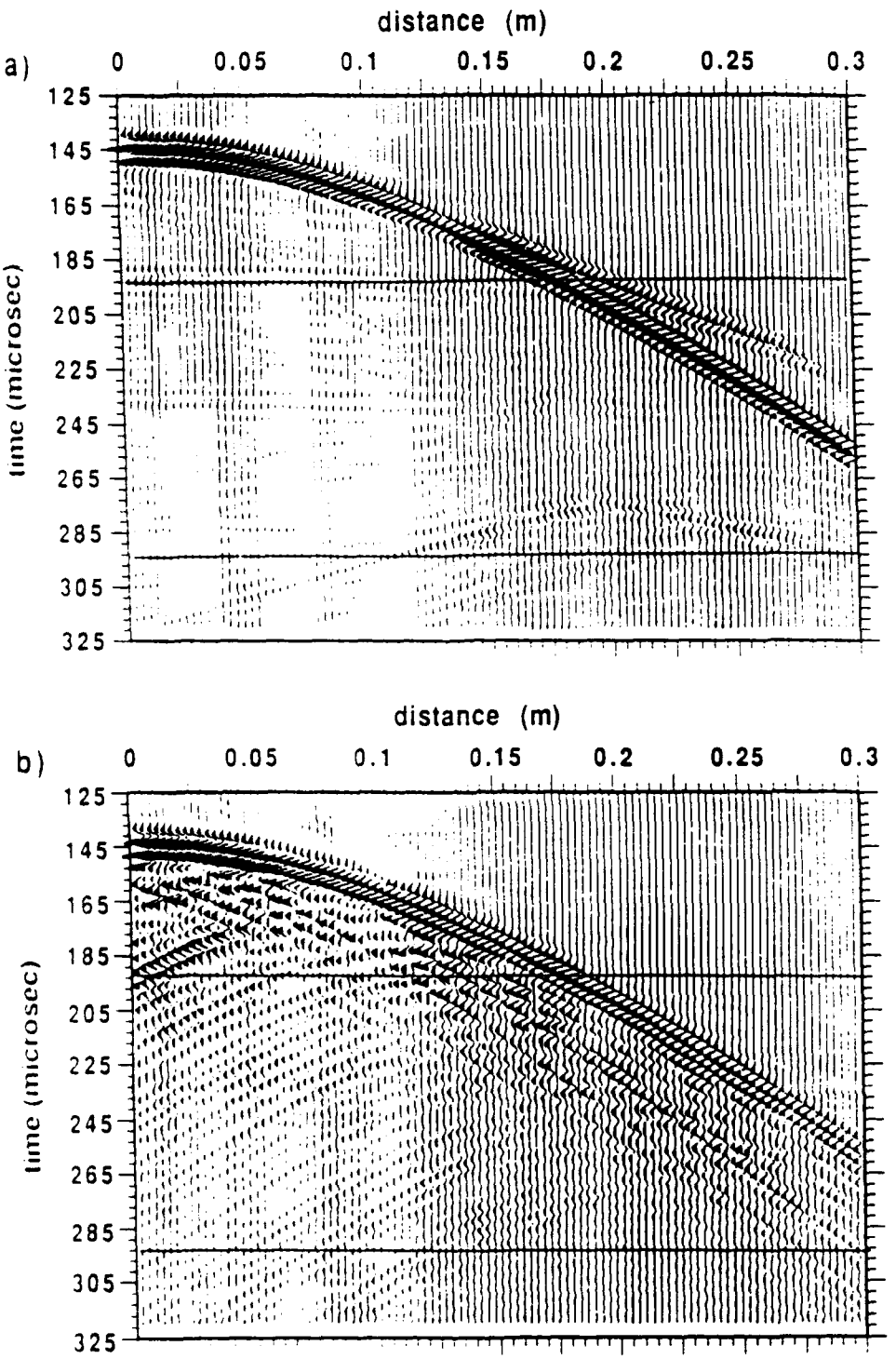

Figure 8: Synthetic seismograms for a volume source over both (a) a flat interface and (b) the two-dimensional grooved interface. Note the large increase in backscattered energy.

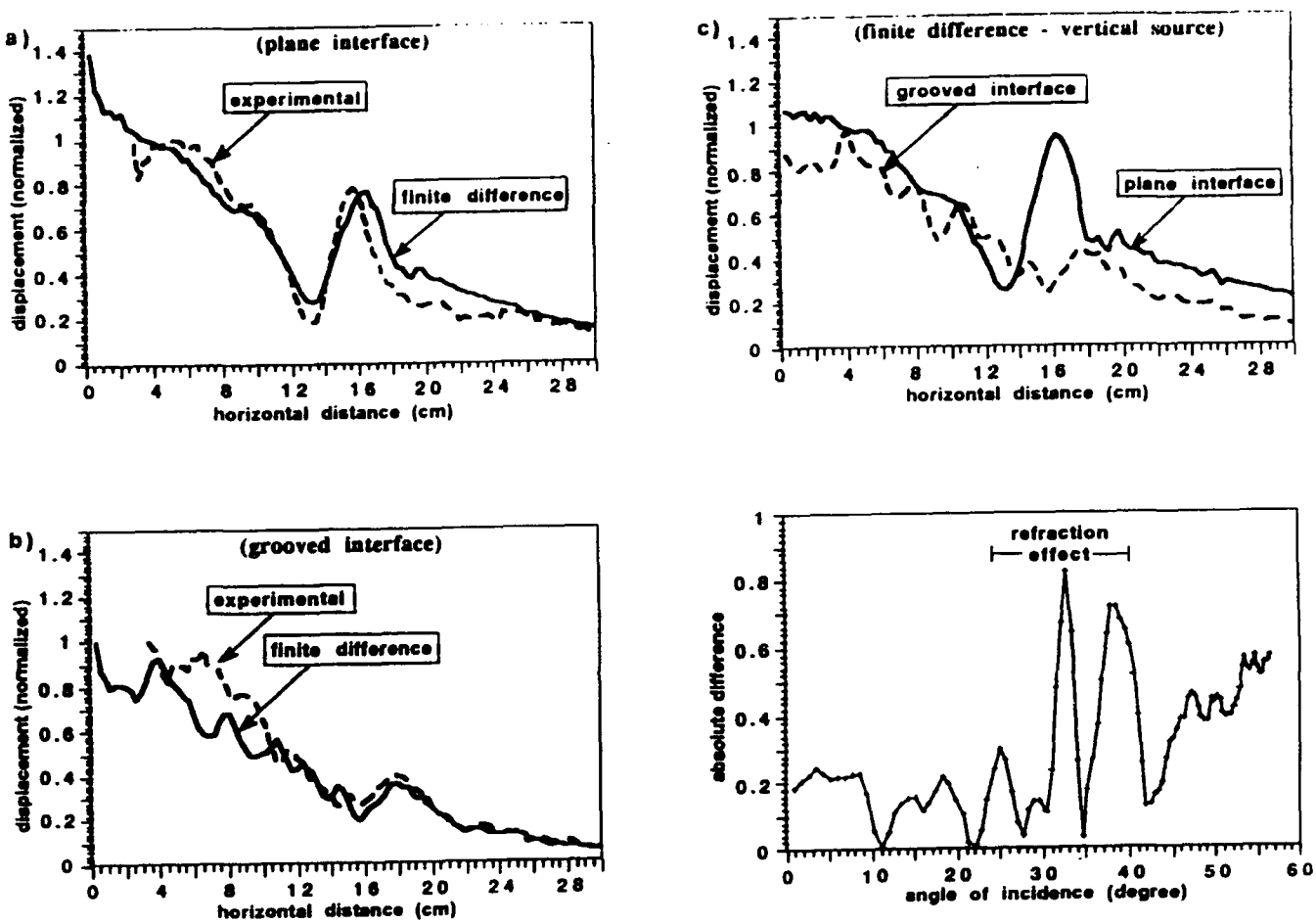

Figure 9: Shows the comparison of finite-difference amplitudes (corrected for the experimental distortions with ultrasonic tank results. The plane layer (a) and the grooved interface (b) cases both match very well. (c) compares the predicted AVD curves predicted by these finite-difference synthetics and gives their relative difference.